Clay mineral evolution and formation of intermediate phases during pedogenesis on picrite basalt bedrock under temperate conditions (Yunnan, southwestern China)

Hanlie Hong [a,b,*], Kaipeng Ji [a], Hetang Hei [c], Chaowen Wang [d], Chen Liu [a], Lulu Zhao [a], Bruno Lanson [e], Chenlei Zhao [a], Qian Fang [a], Thomas J. Algeo [a,f,g]

[a] State Key Laboratory of Biogeology and Environmental Geology, China University of Geosciences, Wuhan 430074, China
[b] School of Earth Sciences, China University of Geosciences, Wuhan, Hubei 430074, China
[c] Yunnan Earthquake Agency, Kunming, Yunnan 650224, China
[d] Gemmological Institute, China University of Geosciences, Wuhan, Hubei 430074, China
[e] Univerisity of Grenoble Alpes, ISTerre, F-38041 Grenoble, France
[f] Department of Geology, University of Cincinnati, Cincinnati, OH 45221-0013, USA
[g] State Key Laboratory of Geological Processes and Mineral Resources, China University of Geosciences, Wuhan, Hubei 430074, China

ARTICLE INFO

ABSTRACT

In order to better understanding clay mineral evolution coupled with geochemical changes during weathering of igneous rocks under temperate conditions, the picrite basalt-derived soil in Dali (South China) was investigated using X-ray diffraction (XRD), X-ray fluorescence (XRF), scanning electron microscope (SEM), and high-resolution transmission electron microscopy (HRTEM) methods. Our results show that smectite and mixed-layer clays occur throughout the weathered soil profile, while discrete kaolinite and illite phases are absent in the soil. From saprolite to topsoil, smectite decreases sharply, while mixed-layer kaolinite/smectite (K/S) and illite/smectite (I/S) clays increase markedly. Clay minerals in the saprolite consist of both dioctahedral and trioctahedral species, while those of the middle to upper profile display a uniform dioctahedral structure. I/S phases are characterized by interstratification of 12-Å smectite and 10-Å illite layers, and K/S phases by interstratification of 12-Å smectite and 7-Å kaolinite layers, with I/S/K clays containing all three layer types. Kaolinization of smectite occurs at the initial stage of weathering, earlier than that of smectite illitization. Desilication and K-fixation of smectite take place simultaneously during advanced weathering, resulting in formation of illitic and kaolinitic phases continuously throughout the developmental history of the soil. Notably high K concentrations in the weathering profile may be related to K-fixing in the interlayer of illite due to smectite illitization in response to more advanced weathering and pedogenic processes, while the increasing K content in the topsoil may be ascribed to fertilizer in land use and uptake of K by plants from deeper soil horizons. Fe_2O_3 and TiO_2 accumulation in the topsoil is probably mediated by microorganisms.

1. Introduction

During weathering and pedogenesis, the initial alteration of basic igneous rocks usually produces smectite, allophane, and imogolite in various environments, which are then transformed into other clay phases, dominated by kaolins and mixed-layer kaolinite/smectite (K/S), as soil formation proceeds (Alexander and Heal, 1974; Kantor and Schwertmann, 1974; Curtin and Smillie, 1981; Glassmann and Simonson, 1985; Righi et al., 1999; Vingiani et al., 2004; Rasmussen et al.,

2010; Perez-Fodich and Derry, 2019). Neoformed smectite has a dioctahedral structure typically of a ferriferous member of the montmorillonite-beidellite series, occurring in the lower soil horizon, while illite and poorly-crystalline kaolinite predominate in the upper soil profile (Kantor and Schwertmann, 1974; Curtin and Smillie, 1981).

Key weathering processes, such as acid hydrolysis and oxidation of bedrock as well as the formation of secondary clay phases, are dependent on bedrock lithology and other soil-forming factors such as climate, topography, and drainage conditions (Chesworth, 1973; Curi and

---

Franzmeier, 1987; Vingiani et al., 2004; Deepthy and Balakrishnan, 2005; Li et al., 2016; Wilson et al., 2017; Perez-Fodich and Derry, 2019). Cool and moist climatic conditions favor the formation of short-range order phases, whereas warm and dry conditions produce smectite, kaolins, and crystalline Fe-oxyhydroxides (Dekayir and El-Maataoui, 2001; Rasmussen et al., 2010; Jiang et al., 2018). Under humid temperate conditions at Killundine, Morvern, Scotland, weathering of fresh basalt initially formed a trioctahedral clay phase that transformed through a mixture of di- and trioctahedral species to a dioctahedral interstratified illite/smectite (I/S) phase with minor hematite and anatase in highly weathered soils (Bain, et al., 1980). In the temperate Middle Atlas, Morocco, weathering of alkali basalt was initially dominated by dissolution of glass and deposition of poorly-crystalline Si-Al products, which then transformed into halloysite, kaolinite, and hematite during enhanced weathering, while illite and vermiculite were regarded as introduced phases that did not originate from the basalt bedrock (Dekayir and El-Maataoui, 2001). A basalt weathering under seasonally wet, temperate climate conditions in Sardinia, Italy yielded mainly K/S clays, with drainage conditions controlling the proportion of kaolinite in the mixed phase (Righi et al., 1999; Vingiani et al., 2004). Also, the ferric smectite layer content in the K/S decreased upward through the soil profile, and kaolinization of smectite took place by complete dissolution of preferentially ferric smectite layers and crystallization of kaolinite layers in the interlayer regions of smectite particles (Curtin and Smillie, 1981; Righi et al., 1999). However, Singer and Armannsson (1999) reported that, in the weathering profile of Pleistocene basalts under moderately humid Mediterranean conditions, smectite was the only clay mineral formed in the saprolite, and the clay fractions of the regolith consisted of smectite, kaolinite, and minor halloysite without intermediate phases.

Various patterns and processes of pedogenesis in basic igneous rocks have also been proposed (e.g., Bain, et al., 1980; Ma et al., 1999; Dekayir and El-Maataoui, 2001; Campodonico et al., 2019; Sulieman et al., 2020). Orhan and Hüseyin (2018) showed that, in a subhumid climate, basalt-derived soils contained dominantly smectite, with minor illite, kaolinite, and vermiculite, and the content of smectite increased with depth in the soil and was controlled by local topography and drainage. Under a temperate Mediterranean-type climate, weathering of basalts produced dominantly smectite with minor kaolin, illite, and palygorskite at lower elevations, whilst kaolin was dominant on local topographic highs (Prudêncio et al., 2002). However, variation in the clay phases of basalt-derived soils has also been attributed to other factors such as hydrothermal alteration during lava cooling (Bain et al., 1980; Pokrovsky et al., 2005), illitization of smectite due to plant uptake of K from deeper soil horizons (He et al., 2008), and influx of allochthonous aeolian material (Dekayir and El-Maataoui, 2001; Rasmussen et al., 2010). Furthermore, Nesbitt and Wilson (1992) claimed that climate conditions affect only the rates but not the mechanisms of chemical weathering of basalts, and that the diversity of clay mineral assemblages formed in basalt-derived soils under a range of climate conditions depends mainly on the steady-state conditions of the climate regime (i.e., chemical weathering *vs* erosion).

Although the weathering of basalt under temperate climate conditions seems to conform to a general pattern of initial formation of smectite and subsequent transformation toward kaolin (Prudêncio et al., 2002), the specific processes of basalt pedogenesis and, especially, the characterization of intermediate phases in basalt-derived soils remain a matter of debate (Bain, et al., 1980; Glassmann and Simonson, 1985; Dekayir and El-Maataoui, 2001; Vingiani et al., 2004; He et al., 2008; Caner et al., 2014; Wilson et al., 2017; Jiang et al., 2018; Perez-Fodich and Derry, 2019; Sulieman et al., 2020). A lack of investigation of the mineralogy of picrite basalts undergoing weathering hinders a comprehensive understanding of the evolution of clay phases and the transformative processes in such pedogenic systems. Temperate climate conditions commonly allow development of a complete, advanced sequence of intermediate weathering phases (Bain, et al., 1980; Vingiani et al., 2004). In this study, analysis of the clay mineralogy and geochemical changes in a soil profile developed on the well-studied basaltic bedrock in the temperate Dali region of Yunnan Province, South China was undertaken in order to address the pattern of pedogenesis and soil mineral evolution during weathering of picrite basalt. The aims of our investigation were: (1) to provide new insights into the pedogenesis of picrite basalt under temperate climate conditions, and (2) to provide additional constraints on reaction pathways for formation of intermediate clay-mineral phases during weathering.
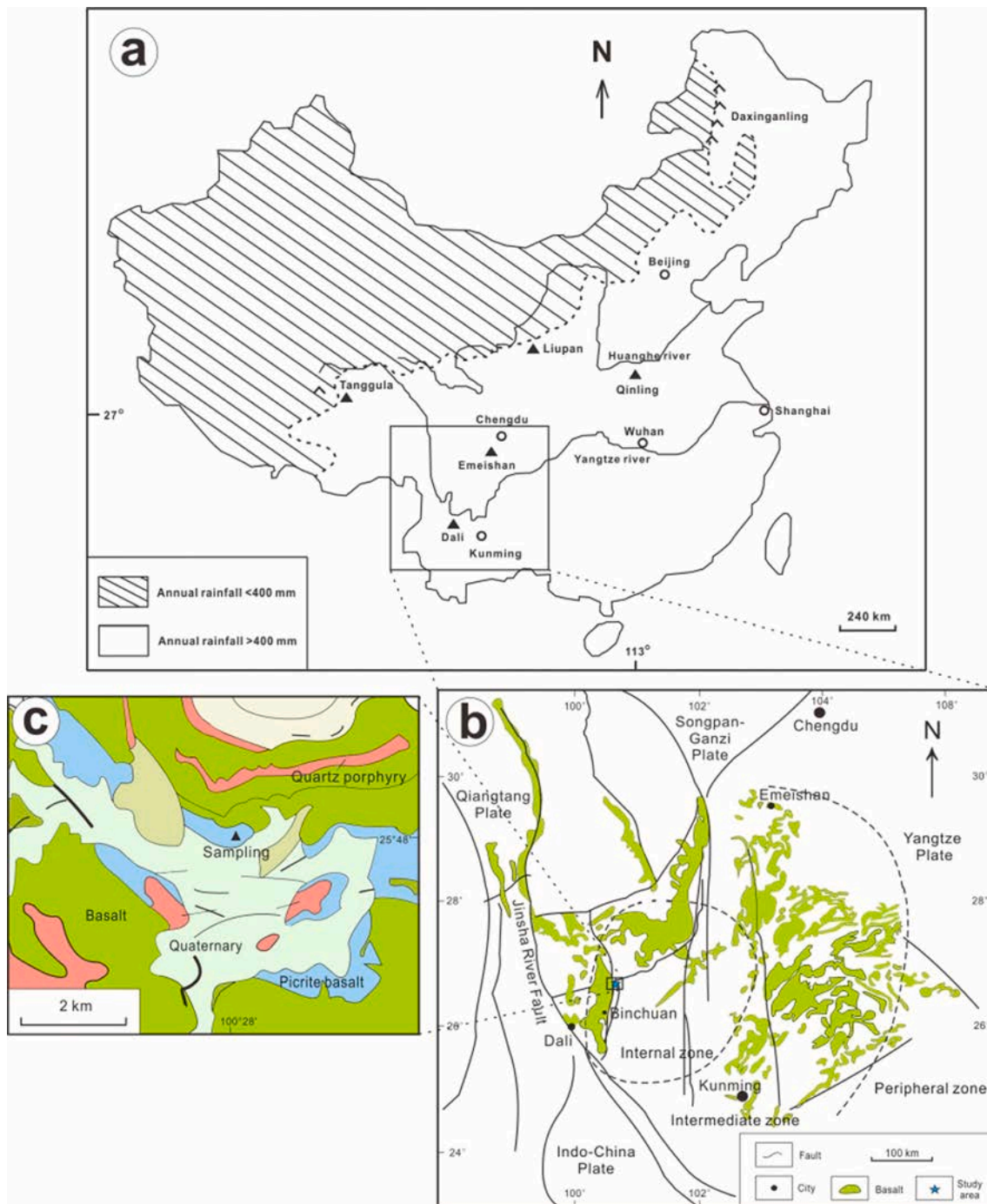
2. Study area

The study area is situated in the central zone of the Emeishan Large Igneous Province, in the southwestern part of the Yunnan-Guizhou Plateau, southwestern China (Fig. 1). The Emeishan basaltic traps, with a cumulative thickness ranging from five kilometers (proximally) to tens of meters (distally), are part of a major large igneous province outcropping mainly in southwestern China over an area in excess of a quarter million square kilometers with a center near Dali (Yunnan) to Miyi (Sichuan) (He et al., 2003). They overlie Late Permian carbonates of the Maokou Formation and are overlain by the Triassic Wujiaping sedimentary sequence (Courtillot et al., 1999; He et al., 2003). The lithology of the Emeishan traps changes slightly as a function of local tectonic setting, occurring as basalt, picrite basalt, alkaline basalt, tholeiite, and minor picrate, trachyandesite, and trachyte (Hou et al., 1999).

The landscape of the Dali area consists of plateaus, mountains, and intermontane basins, including geomorphic units representing high mountain canyons, alluvial fans, lakeside slopes, broad valleys, and complex terrains, at altitudes ranging from 1340 to 4122 m above sea level. It has a low-latitude plateau monsoonal climate characterized by a mean annual temperature of 15.1 °C (mean monthly temperatures range from 3.7 to 28.9 °C) and a mean annual precipitation of ~ 700 mm. The study section is located at Daying town (100°28′E, 25°48′N), Dali City, Yunnan Province, South China, at an altitude of 1722 m. Eolian sediments have not been observed in Dali, as monsoonal winds transport eolian materials only as far southward as the middle of China (Qiao et al., 2011). The vegetation of the study area consists dominantly of alpine herbs and the high-altitude shrubs belonging to the genus *Quercus*, and human land use is constrained mainly to maize cultivation owing to the limited rainfall. Soil developed at the footslope position, where excavation for a water channel provided access to a 4.6-m-thick soil profile overlying unweathered picrite basalt bedrock.

3. Materials and methods

3.1. Field sampling

The topsoil (Layer 1, 0–40 cm) displays a porous and loose crumb structure and is brownish gray in color, consisting mainly of sandy clays and minor gravels, with relatively abundant organic matter and plant roots. A reddish-brown silty clay horizon (Layer 2, 40–100 cm) is present under the topsoil, exhibiting a homogeneous crumb structure and containing minor plant roots. The underlying horizon (Layer 3, 100–160 cm) is light gray in color and blocky in structure, having short white clay veins or spots. A thick grayish-brown clayey gravel saprolite horizon (Layer 4, 160–380 cm) is present beneath Layer 3. It is composed dominantly of clays and gravels of incompletely weathered bedrock, with minor amounts of Fe-Mn nodules. The bedrock is greyish-green picrite basalt that exhibits an amygdaloidal structure (Fig. 2). Representative samples (~1 kg each) were collected from the weathering profile at 10–20 cm intervals in the upper portion (0–1.6 m) and at 40 cm intervals in the saprolite (1.6–3.8 m) of the lower portion, yielding a total of 18 samples.

Fig. 1. Location and geologic setting. (a) Climate map showing mean annual precipitation in China; (b) Regional geological map showing the distribution of the Emeishan Large Igneous Province; (c) Detail of study area.

3.2. Selected chemical and mineralogical analyses

Soil pH measurements were performed in distilled water using a glass electrode in a 1:2.5 soil/water suspension. The cation exchange capacity (CEC) determination of soil samples was performed using the sodium chloride–ethanol method of Chen et al. (2000). For total organic carbon (TOC) analysis, the soil samples were ground to pass through a 200-mesh sieve. The powdered samples were then reacted with hydrochloric acid (0.1 mol L^{-1}) overnight to remove carbonate. TOC measurement was performed on a Vario Macro Cube carbon analyzer. For X-ray diffraction (XRD) analysis, whole-rock samples were air-dried at 60 °C overnight and then ground manually to powder using an agate

mortar and pestle. The mineral contents of the whole-rock samples were estimated using the reference intensity ratio approach with admixture of corundum as the internal standard (Hillier, 2000). The mixing powder samples were prepared by mounting the powders into sample holders using a back-press technique. The characteristic peaks of minerals used in our calculation were 3.34 Å (quartz), 3.19 Å (plagioclase), 3.51 Å (anatase), 2.97 Å (clinopyroxene), 2.90 Å (pumpellyite), and 2.70 Å (hematite), 15 Å (smectite), and 7.40 Å (kaolinite/smectite), respectively. The relative standard deviation of the semi-quantitative method is usually < 15 %.

The clay fraction (<2 μm) was extracted using the sedimentation method (Jackson, 1978), and an oriented clay-fraction sample was

Fig. 2. Photographs of the Dali weathering soil profile developed on picrite basalt. (a) A full view of the soil profile. (b), (c), (d), (e), and (f) are close-up photographs showing Layers 1, 2, 3, 4, and the bedrock, respectively. Scale provided by 13-cm-long marker.

prepared for clay mineralogical investigation by pipetting the clay suspension, with a solid-to-liquid ratio of around 1:25, onto a glass slide that was subsequently air-dried at ambient temperature. In order to determine swelling clay components, the oriented clay samples were treated with ethylene glycol in a sealed glass desiccator heated at 65 °C for 4 h in an electronic oven. XRD analysis was performed on a Panalytical X'Pert PRO DY2198 diffractometer with Ni-filtered Cu Kα radiation. The instrument was operated at 40 kV tube voltage and 35 mA

tube current conditions, with the slit system of 1° divergence slit, 1° anti-scatter slit, and 0.3 mm receiving slit, and the XRD patterns were collected from 3° to 65° 2θ at a scan rate of 4° 2θ min⁻¹ and a step size of 0.02° 2θ.

For observation of the (0 6 0) peak of clay phases, the non-oriented clay samples were prepared using the back-press method. The layer content of the end member in a mixed-layer clay phase and the relative abundance of clay phases in the sample were estimated using the

NEWMOD II program (Reynolds and Reynolds, 1996), which was performed simultaneously for the XRD patterns of both glycolated and Ca-saturated clay samples.

3.3. Major element compositions and mass balance calculations

The chemical compositions of the samples were measured using X-ray fluorescence (XRF). Prior to preparation of the fused XRF pellets, measurement of loss-on-ignition (LOI) was performed by drying a sample aliquot in an oven at 105 °C for 2 h and then heating 1 g of the dried sample to 1000 °C for 1.5 h. The LOI value was calculated from the difference in weight between the sample aliquots heated to 105 °C and to 1000 °C. Preparation of fused pellets for XRF measurement was as follows: a 5-g aliquot of sample was dried in an electronic oven at 60 °C overnight and then manually ground to a fine powder with a grain size of<0.074 μm (200 mesh) for generation of fused XRF pellets. Major element compositions were analyzed on an XRF-1800 SHIMADZU sequential X-ray fluorescence spectrometer. The detection limit was generally ~ 0.01 wt%, and the relative standard deviation was usually < 1 %.

The degree of mobilization of each element in the weathering profile was estimated through a mass balance calculation using Al as an immobile reference element (Campodonico et al., 2019) and the chemical composition of the unaltered bedrock as the starting mass. The formula for this calculation is: $C_{GL} = [C_S /Al_S] \times Al_{BR} - C_{BR}$, where C_{GL}, C_S, and C_{BR} represent the gain or loss (GL) of the element of interest as well as its concentration in the soil sample (S) and the unaltered bedrock (BR), and Al_S and Al_{BR} represent the aluminum concentrations of the sample and bedrock, respectively.

3.4. SEM and HRTEM observations

Small chips (~1 cm) of whole-rock samples were selected and then gold-coated. Scanning electron microscope (SEM) observation was undertaken on a Hitachi SU8010 field emission scanning electron microscope, equipped with an Octane Super X-ray energy-dispersive (EDS). The instrument was operated at an accelerating voltage of 20 kV and a probe current of 2nA, with a magnification up to 8×10^5 and a resolution of secondary electron image of 1.0 nm.

For high resolution transmission electron microscopy (HRTEM) observation, the air-dried clay fraction was immersed in methanol solution and then ultrasonically dispersed for 10 min, after which the clay material was collected with a copper net and dried under an infrared light. HRTEM observation was performed on a Tecnai G2 20 S-TWIN high-resolution transmission electron microscope, equipped with a GENESIS 2000 X-ray energy-dispersive (EDS). The instrument was operated at the condition of 160 kV accelerating voltage, with a beam spot size of 1.5 nm, a point resolution of 0.24 nm, and a line resolution of 0.14 nm.

4. Results

The pH, TOC, and CEC values of the soil samples are listed in Table 1. The XRD patterns of representative soil samples are shown in Fig. 3a and

their mineral compositions are tabulated in Table 1. The clay mineral components and their relative proportions were obtained from fitting XRD traces of the glycolated samples (Fig. 4), and were further confirmed by fitting the air-dried samples (Fig. 5), and their relative contents are listed in Table 2.

4.1. Physical and chemical properties and mineral compositions of the soil

Mineral components in the soil profile are mainly clay minerals, plagioclase, quartz, and hematite. Mineral abundances displayed only small changes between samples from the same soil horizon but varied considerably between samples from different soil layers, as reflected by intensities of their characteristic peaks of the minerals (Fig. 3a). The bedrock consists dominantly of pumpellyite (2.90, 3.79, 4.67, 2.74, 2.52 Å) and clay minerals (15.0 Å), with minor amounts of plagioclase (3.18 Å), quartz (3.34, 4.26, 1.82 Å), and hematite (2.70, 2.52, 1.485 Å) and trace clinopyroxenes (2.97 Å), suggesting that the picrite basalt bedrock has undergone low-grade burial metamorphism. In addition, the XRD profiles of selected clay-fraction samples show that clay phases from the middle to upper soil profile exhibit a uniform dioctahedral structure (1.50 Å), whereas those from the saprolite horizon consist of both di- (1.50 Å) and trioctahedral (1.54 Å) species (Fig. 3b).

Clay species in the Dali soil profile are dominantly smectite, K/S, and I/S, characterized by the 14.8 Å peak in the XRD patterns of the untreated whole-rock samples (Fig. 3), which expanded to around 17 Å after glycolation (Figs. 4-5). Smectite accounts for the 17-Å peak, and the notable decrease in intensity upward in the soil profile indicates a gradual decrease in smectite content. I/S accounts for the bump peak at ~ 8.5–8.8° 2θ, which is evident for the upper samples but not visible for the deeper samples, indicating an upward increase of this mineral phase. The 7.4-Å peak (~12° 2θ) is ascribed to a K/S phase with no contribution from discrete kaolinite, which requires two sub-populations to be fitted properly since it is a broad reflection (Table 2). K/S occurs throughout the soil profile, forming two sub-populations marked by higher proportions and lower proportions of kaolinite layers, while I/S occurs dominantly in Layers 1, 2, and 3 but is almost absent in the Layer 4. Overall, smectite decreases concurrently with increases in I/S clays upward within the soil profile, and K/S clays are notably less abundant in the lower samples relative to the upper samples (Table 2).

4.2. Geochemical composition of the soil

The Dali soil shows marked variations in geochemical composition among its component soil layers, but only small differences between samples from the same horizon (Table 3; Fig. 6). Samples from the lower profile, especially the Layer 4, contain relatively more SiO_2 (49.6–51.7 %) compared to those from the upper profile (43.0–46.8 %). TiO_2 contents are notably high (3.5–3.6 %) in the Layer 1. Al_2O_3 is modestly concentrated in the middle profile (Layers 2 and 3; 19.0–23.5 %) relative to.

Layer 1, Layer 4, and bedrock (15.6–18.2 %). TFe_2O_3 is highest in Layer 1 (18.1–18.2 %), with intermediate and uniform values in Layers 2 and 3 (15.5 %) and relatively lower values in the lower profile (Layer 4, 12.8–14.2 %; bedrock, 11.9 %). The MgO and CaO contents exhibit

Table 1
Some selected morphological, physical and chemical attributes, and mineral compositions of the soil developed from Dali picrite basalt weathering.

Soil layer	Sample	Color	Texture	Structure	pH	TOC (wt%)	CEC (cmol(+)/kg)	Mineral content (wt%)						
								Clays	Pl	Qtz	Ant	Cln	Hm	Pum
Layer 1	DYX-01	5 YR5/1	Sandy clay	Crumb	4.9	1.64	24.3	50	17	7	3	2	16	5
Layer 2	DYX-05	5 YR5/6	Silty clay	Crumb	5.7	1.07	54.7	65	18	2	2	3	10	/
Layer 3	DYX-11	7.5 YR8/1	Clay	Blocky	6.0	0.59	34.5	57	19	5	2	6	11	/
Layer 4	DYX-16	7.5 YR6/2	Clayey gravel	Blocky	6.8	0.83	41.1	54	23	2	2	5	14	/
Bedrock	DYX-18	Grayish green	/	/	/	/	/	13	2	24	2	7	8	44

Notes: Pl-plagioclase; Qtz-quartz; Cln-clinopyroxene; Pum-pumpellyite; Hm-hematite; Ant-anatase; "/"-not measured or not detected.
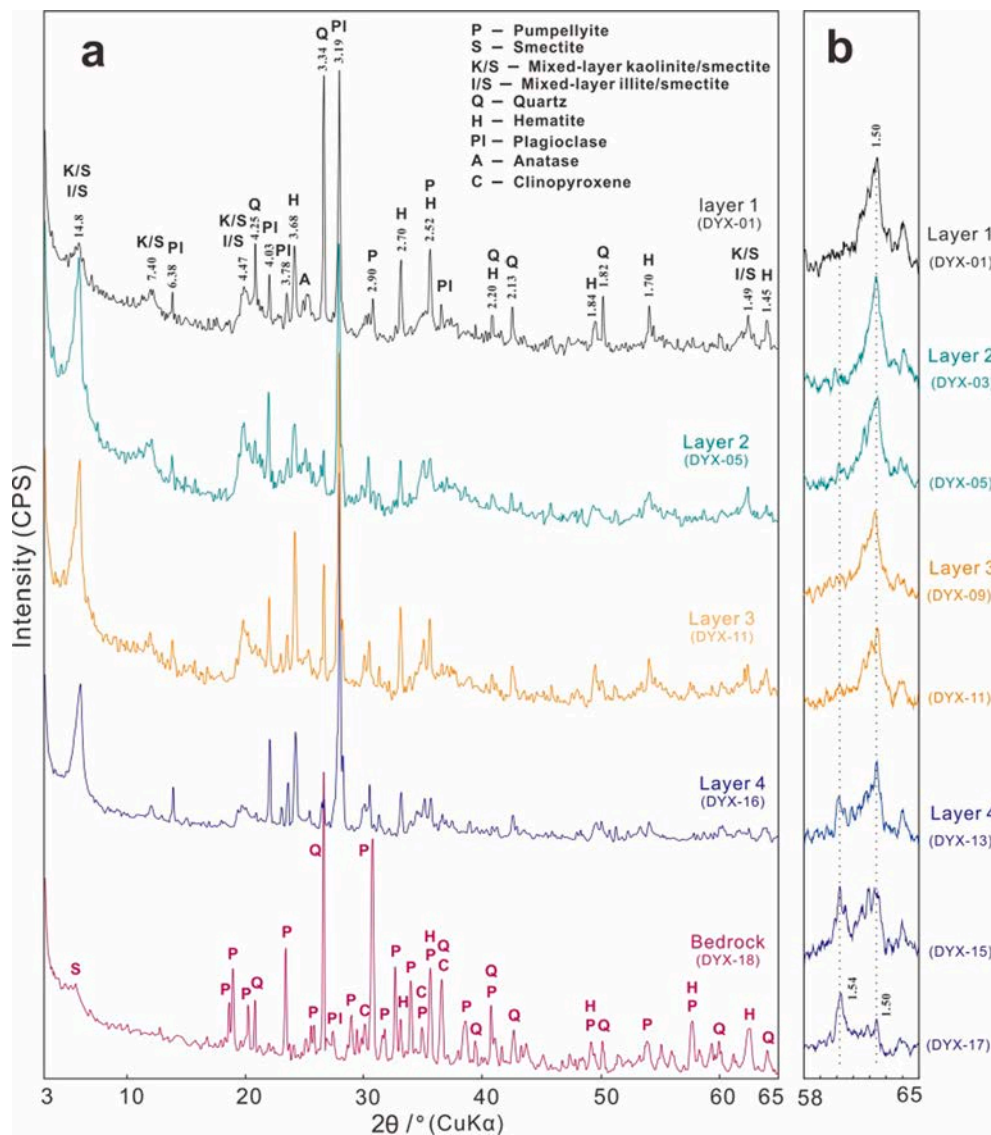
Fig. 3. XRD patterns of representative samples of the Dali soil profile. (a) Whole-rock samples; (b) (0 6 0) reflections of XRD patterns of clay fractions.

downward increases from 1.7 to 4.8 % and from 1.1 to 3.3 %, respectively. Moreover, the CaO content of the bedrock is extremely high (to 19.5 %). The Na_2O content of the soil samples shows a downward increase from 1.1 to 4.8 %, whereas the K_2O content exhibits a downward decrease from 0.9 to 0.1 %. However, the Na_2O and K_2O contents of the bedrock are markedly lower (0.02 % and 0.01 %, respectively). The P_2O_5 content of the soil samples varies from 0.1 to 0.3 %, but Layer 1 and Layer 4 contain generally more P_2O_5 relative to the other soil layers.

4.3. SEM observations

In general, clay flakes in Layer 1 display a relatively smooth and flat basal (0 0 1) plane and exhibit a generally poorly-developed pseudo-hexagonal or plate-like outline (Fig. 7a). Also, the edges of clay mineral flakes are relatively straight, similar to the common morphologies of kaolinite and illite. Clay mineral grains in Layer 2 often.

exhibit relatively well-developed euhedral pseudo-hexagonal morphology with a smoother basal (0 0 1) plane and straighter edges (Fig. 7b), indicating higher crystallinity relative to those of the topsoil. In the Layer 3, although most of the clay mineral grains display a relatively smooth basal (0 0 1) plane, clay minerals usually develop curled edges and thus typically exhibit wave-shaped outlines (Fig. 7c),

consistent with the morphologies of typical K/S and I/S clays (Hong et al., 2008; 2017).

Clay minerals in the Layer 4 display three different morphologies: (1) Abundant clay particles that are extremely small in comparison with those in the overlying soil layers; they display ragged outlines (Fig. 7d) and often replace basalt particles. (2) Clay minerals that are larger and typically develop curled edges in fissures or in the interstitial spaces among residual basalt particles, suggesting the occurrence of smectite or I/S clays (Fig. 7d). (3) Clay minerals with a honeycombed polygonal pattern, indicative of neoformed smectite (Fig. 7e); their distinctive curled edges and interwoven structure, as well as their presence primarily in open cavities, are suggestive of smectite that crystallized from solution during weathering. The picrite basalt bedrock shows generally a solid glass structure, with only rare small vesicular pores (Fig. 7f).

4.4. HRTEM observations

Clay particles generally display a wave-shaped morphology and have a relatively thin and poorly developed (0 0 1) surface (Fig. 8a). The edges of these particles are typically curved and curled, consistent with the characteristic morphologies of smectite, K/S, and I/S clays (Van Der Gaast et al. 1986; Hong et al., 2012). However, in samples from the
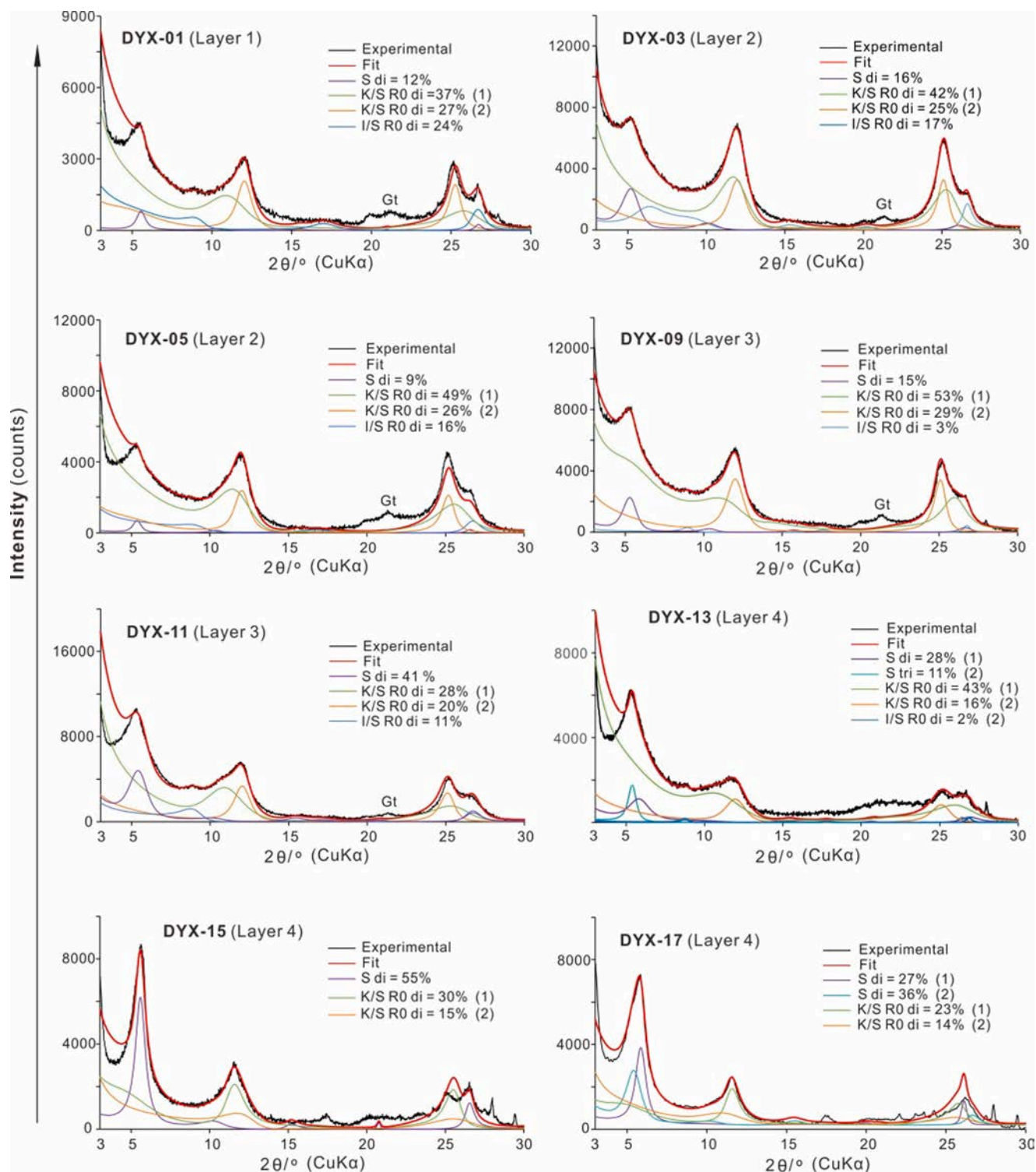
Fig. 4. Fitted XRD patterns of glycolated clay fractions showing the stacking structures of mixed-layer clay species and their relative contents. Abbreviations: K/S: mixed-layer kaolinite/smectite; I/S: mixed-layer illite/smectite; S: smectite; Gt: goethite; di: dioctahedral; tri: trioctahedral.

upper soil profile, some of the clay flakes exhibit relatively euhedral morphologies in long, plate-shaped crystals with straight outlines along the (0 0 1) dimension, consistent with the crystal morphology of strongly illitized I/S clays (Fig. 8b). Clay flakes with relatively well-developed euhedral pseudo-hexagonal outlines are also present in these soil samples (Fig. 8c). The basal (0 0 1) planes of clay particles are smooth and flat, and their lateral surfaces (1 1 0) and (0 1 0) are clearly defined with straight edges, similar to the morphology of kaolinite.

The margins of clay particles with thick and lath-shaped morphologies usually display straight lattice fringes with 10-Å spacing, in agreement with those of illite layers. However, the 10-Å fringes are often intercalated with 12-Å smectite layers, indicative of the presence of interstratified I/S (Fig. 8d). For clay particles with relatively thin and wave-shaped morphology, the 12-Å fringes are often irregularly interstratified with 7-Å fringes, suggesting the occurrence of K/S (Fig. 8e). In addition, the 12-Å layers are occasionally observed to be interstratified
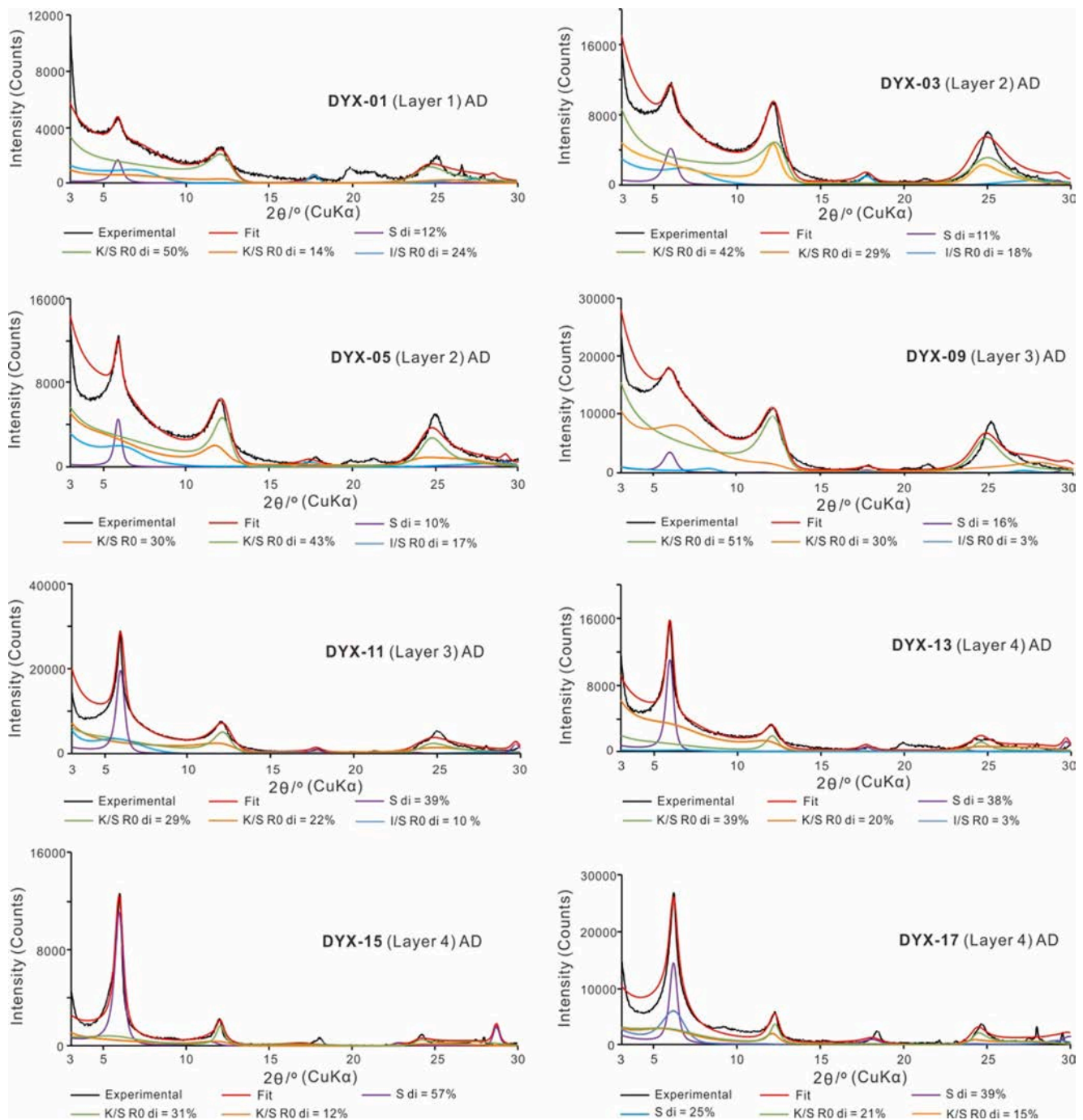
Fig. 5. Fitted XRD patterns of air-dried clay fractions showing compatible clay mineral compositions to those of the glycolated samples (Fig. 4).

with both 7-Å kaolinite layers and 10-Å illite layers (Fig. 8f), indicating a mixed-layer smectite, illite, and kaolinite (I/S/K) stacking structure.

5. Discussion

5.1. Clay mineral evolution through the weathering profile

As a result of burial metamorphism, the Dali picrite basalt bedrock consists mainly of pumpellyite, smectites, hematite, quartz, and minor amounts of plagioclase, clinopyroxenes, and anatase (Fig. 3; Table 2). The Emeishan basalts commonly display amygdaloidal and vesicular structures (Hou et al., 1999). This volcanic rock was subjected to burial diagenesis during the Late Permian, producing mainly pumpellyite,

smectite, and hematite (Mevel, 1981; Inoue and Utada, 1991; Mirabella et al., 2005; De Rosa et al., 2016). The picrite basalt rock consists mainly of SiO_2, FeO, MgO, CaO, Al_2O_3, corresponding to the general mineral compositions of olivine and plagioclase. The burial alteration process can be described as the following reaction equation: $3MgFeSiO_4$ (olivine) + $5CaAlSi_2O_8$ (plagioclase) + $12H^+$ → $Ca_4MgAl_5[Si_2O_7]_2[SiO_4]_2(OH)_5 \cdot H_2O$ (pumpellyite) + $CaMg_2[Si_4O_{10}]$ $(OH)_2 \cdot 1.5H_2O$ (smectite) + $1.5Fe_2O_3$ (hematite) + $3SiO_2$. Tectonic uplift has exposed the Emeishan basalts, and supergene weathering has taken place since the Late Triassic. Initial alteration of the bedrock entailed dissolution of pumpellyite (Table 3; Fig. 6), followed by precipitation of newly formed smectite clays in small fissures and pores in the bedrock (Fig. 7e,f,g). The poorly-crystalline small clay grains are often

8

Table 2

Clay mineral compositions of representative soil samples from the Dali picrite basalt weathering profile (wt%).

Soil layer	Sample	Smectite	I/S (Illite layer content)	K/S (1) (Kaolinite layer content)	K/S (2) (Kaolinite layer content)	Total K/S
Layer 1	DYX-01	12	24 (79 %)	37 (75 %)	27 (87 %)	64
Layer 2	DYX-03	16	17 (33 %)	42 (86 %)	25 (89 %)	67
	DYX-05	9	16 (71 %)	49 (82 %)	26 (89 %)	75
Layer 3	DYX-09	15	3 (90 %)	53 (63 %)	29 (90 %)	82
	DYX-11	41	11 (85 %)	28 (87 %)	20 (92 %)	48
Layer 4	DYX-13	39 (28 di + 11 tri)	2 (93 %)	43 (69 %)	16 (87 %)	59
	DYX-15	55 (33 di + 22 tri)	/	30 (78 %)	15 (84 %)	45
	DYX-17	64 (22 di + 42 tri)	/	23 (75 %)	13 (77 %)	36

Notes: I/S: mixed-layer illite/smectite; K/S: mixed-layer kaolinite/smectite, (1) relatively weak kaolinization and (2) relatively strong kaolinization; "/": undetected; di: dioctahedral; tri: trioctahedral.

replacements of pumpellyite aggregates as the latter alter into smectite (Fig. 7h). Dissolution of bedrock in the first stage of weathering yielded relatively less mobile Si-Al-rich materials in fissures and pores (Fig. 7g) and subsequently crystallized to larger smectite flakes with curled edges in honeycombed polygonal aggregates (Fig. 7e,f).

Although smectite is typically the clay-mineral phase in thermodynamic equilibrium with soil solutions during basalt weathering, microenvironmental conditions can act as kinetic influences on clay-mineral evolution that yield different products from thermodynamic predictions (Ziegler et al., 2003). Microenvironments such as cavities and cracks favor rapid uptake of Al released by poorly-crystalline Si-Al-rich materials (Fig. 7c) and thus facilitate smectite-to-kaolinite transformations. At Dali, smectite is the dominant (39–64 %) secondary clay species in the saprolite horizon, but it decreases in the middle to upper soil profile due to transformation of smectite to mixed-layer K/S. The limited transformation of smectite to I/S clay is probably attributable to the low K content (0.01 %) of the bedrock (Tables 2 and 3). Well-drained conditions usually favor development of kaolinitic soils, whereas poorly-drained environments formation of smectitic Vertisols (Kantor and Schwertmann, 1974; May et al., 1986; Vingiani et al., 2004). In the Dali soil profile, transformation of smectite to K/S and I/S clays was most common in pores (Fig. 7b, c, d). The clay mineral assemblage of mixed-layer K/S and I/S clays, smectite, and Fe-oxides, together with plagioclase and trace pumpellyite, suggests that smectite layers experienced desilication and transformed preferentially to kaolinitic and illitic phases (Glassmann and Simonson, 1985; Righi et al., 1999; Wilson et al., 2017). However, the dominance of K/S and I/S clays in association with minor discrete smectite, as well as a lack of discrete kaolinite and illite through the Dali soil profile, is probably indicative of early-stage desilication within the soil (Figs. 3 and 4; Table 2). Also, the occurrence of plagioclase and absence of gibbsite at Dali confirm a low weathering intensity due to limited acid leaching during basalt alteration, consistent with its significantly low CIA values (Bakker et al., 1996; Vingiani et al., 2004; He et al., 2008; Perez-Fodich and Derry, 2019).

Upward within the Dali soil profile, from Layer 4 to Layer 2, I/S and K/S clays generally increase while smectite concurrently decreases, associated with increasing proportions of illitic and kaolinitic layers in I/S and K/S clays, respectively (Table 2). The intercalation of 12-Å smectite and 10-Å illite layers in I/S clays is indicative of illitization of

Table 3

Major element chemistry and CIA and MIA indices of alteration of soil samples from the Dali picrite basalt weathering profile (wt%).

Soil layer	Sample number	SiO$_2$	TiO$_2$	Al$_2$O$_3$	TFe$_2$O$_3$	MnO	MgO	CaO	Na$_2$O	K$_2$O	P$_2$O$_5$	LOI	SUM	CIA	MIA	Zr (10^{-6})	TiO$_2$/Al$_2$O$_3$	Zr/TiO$_2$
Layer 1 (0–40 cm)	DYX-01	45.59	3.47	17.50	18.15	0.28	1.75	2.30	1.81	0.85	0.32	7.63	99.65	72	44	388	0.198	0.011
	DYX-02	44.73	3.56	18.22	18.22	0.27	1.66	1.90	1.66	0.83	0.25	8.21	99.52	74	48	376	0.195	0.011
Layer 2 (40–100 cm)	DYX-03	43.03	2.43	23.50	15.32	0.19	1.97	1.06	1.06	0.46	0.10	10.74	99.84	85	71	257	0.103	0.011
	DYX-04	45.14	2.29	21.50	14.81	0.18	2.54	1.20	2.16	0.36	0.09	9.19	99.45	78	56	236	0.107	0.010
	DYX-05	45.30	2.43	21.11	15.33	0.21	2.82	1.45	2.16	0.36	0.12	8.91	100.20	76	52	245	0.115	0.010
	DYX-06	44.90	2.44	21.23	15.44	0.21	3.17	1.48	1.82	0.34	0.14	9.16	100.24	78	56	232	0.115	0.010
	DYX-07	44.36	2.34	21.85	15.25	0.20	3.08	1.32	1.58	0.35	0.13	9.60	100.05	80	60	228	0.107	0.010
	DYX-08	44.37	2.29	22.07	15.26	0.18	3.17	1.21	1.15	0.33	0.10	9.95	100.07	83	68	222	0.104	0.010
Layer 3 (100–160 cm)	DYX-09	44.19	2.32	22.42	15.54	0.17	2.74	1.10	1.19	0.35	0.08	10.10	100.21	84	68	227	0.103	0.010
	DYX-10	46.77	2.18	20.66	14.49	0.18	3.01	1.22	2.42	0.29	0.08	8.55	99.86	76	52	212	0.106	0.010
	DYX-11	49.06	2.06	19.02	14.58	0.15	2.88	1.75	3.57	0.19	0.17	6.74	100.16	67	35	194	0.108	0.009
Layer 4 (160–380 cm)	DYX-12	49.60	2.10	18.15	14.18	0.15	2.94	2.57	4.70	0.16	0.30	5.17	100.01	59	18	184	0.116	0.009
	DYX-13	51.66	1.94	17.42	12.82	0.17	3.21	3.25	4.45	0.15	0.26	4.81	100.14	56	13	170	0.111	0.009
	DYX-14	50.29	1.97	16.16	13.35	0.22	4.79	3.29	4.16	0.09	0.28	5.26	99.85	56	11	166	0.122	0.008
	DYX-15	50.45	2.01	16.02	13.62	0.19	4.11	3.03	4.46	0.11	0.26	5.04	99.30	55	11	171	0.125	0.009
	DYX-16	50.54	2.06	15.64	14.06	0.18	4.56	2.92	4.84	0.12	0.30	4.74	99.96	54	8	171	0.132	0.008
	DYX-17	49.95	1.94	16.85	13.28	0.21	4.45	3.00	4.18	0.13	0.27	5.51	99.78	57	15	388	0.115	0.008
Bedrock	DYX-18	41.73	1.74	16.58	11.86	0.12	2.40	19.51	0.02	0.01	0.29	5.20	99.44	32	15	376	0.105	0.008

Notes: LOI is loss on ignition; CIA = (Al$_2$O$_3$ / (Al$_2$O$_3$ + CaO*+K$_2$O + Na$_2$O) × 100 %; MIA = 2 × (CIA − 50); Fe in all Fe$_2$O$_3$.
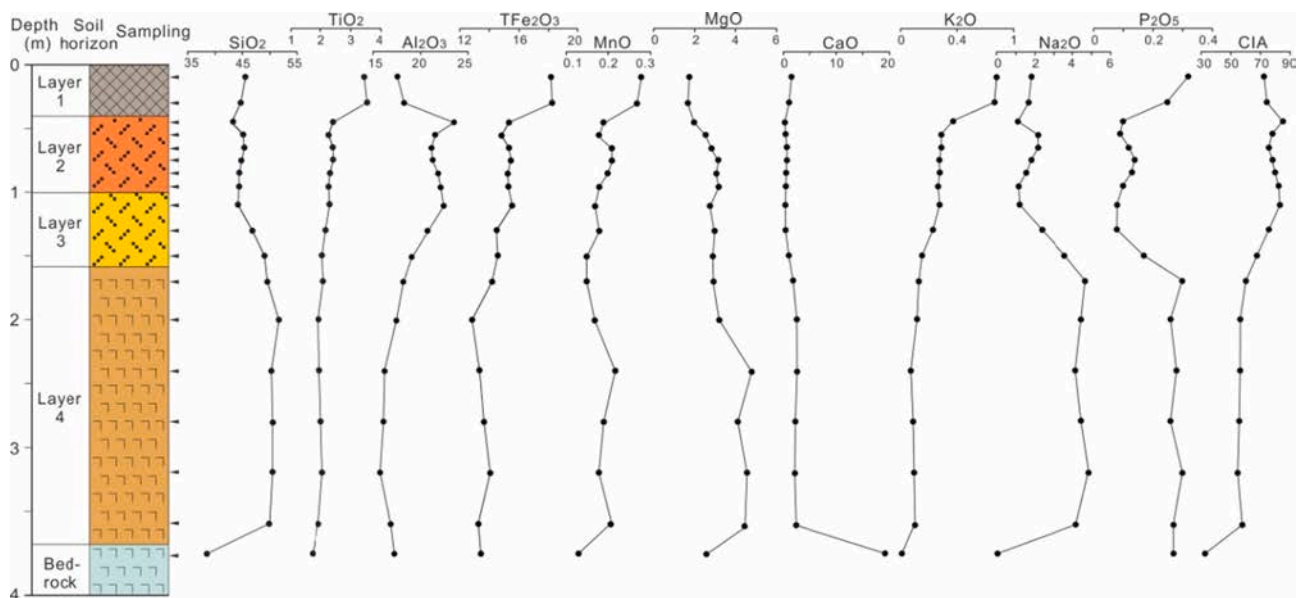
Fig. 6. Changes in major element contents (wt%) and CIA through the Dali picrite basalt weathering soil profile.

smectite due to K-fixation (Fig. 8d), and the random intercalation of 12-Å smectite and 7-Å kaolinite layers in clay particles suggests kaolinization of smectite due to intense weathering (Fig. 8e). The interstratification of 12-Å smectite, 10-Å illite, and 7-Å kaolinite layers reflects formation of mixed-layer I/S/K clays (Fig. 8f), probably due to simultaneous transformation of smectite to illite and kaolinite as weathering proceeded.

The upward decrease in smectite through the weathering profile is clearly due to the kaolinization and illitization of this mineral during the weathering process (cf. Orhan and Hüseyin, 2018). In wide climate conditions, smectite and smectitic interstratifications are common clay mineral assemblages in basalt-derived soils (Bain, et al., 1980; Eggleton et al., 1987; Righi et al., 1999; Vingiani et al., 2004; Barbera et al., 2008; Perez-Fodich and Derry, 2019). In the Dali soil profile, the markedly higher K/S content of Layer 2 and the upper Layer 3 compared to other soil layers (Table 2) is consistent with their relatively greater penetrative condition in the soil profile, and the presence of smectite, K/S, I/S, and I/K/S clays is attributable to relatively weak chemical weathering under temperate, low-rainfall conditions. An increase in the kaolinitic and illitic components of a soil usually causes a decrease in cation-exchange capacity, since the CEC of a soil is dependent mainly on its clay content—especially that of expandable phases (Bain et al., 1980; He et al., 2008; Babechuk et al., 2014). The high CECs of the Dali soil (24.3–54.7 cmol/kg) agree well with the presence of smectite, K/S, and I/S clays (Table 2). Unlike previously studied basalt weathering profiles (e.g., Curtin and Smillie, 1981; Lessovaia et al., 2016; Van Ranst, et al., 2020), clay mineral phases at Dali exhibit structural variation linked to weathering intensity: the weakly weathered saprolite horizon is characterized by a mixture of di- and trioctahedral species, whereas clays in the middle to upper profile have a more uniform dioctahedral structure due to intense weathering (Fig. 3). These changes in clay-mineral structure, which are associated with an increase of Al and a decrease of Mg, probably reflect the replacement of Mg by Al and the oxidation of Fe^{2+} to Fe^{3+} during kaolinization and illitization of smectite in the upper part of the soil profile.

Although the mechanism of transformation of tri- and dioctahedral clay minerals to dioctahedral mixed-layer clay minerals remains poorly understood, it is probably associated with the alteration of smectite to kaolinite in the Dali soil (Righi et al., 1999; Ryan and Huertas, 2009). The neoformed montmorillonite in the saprolite horizon is dominated by migration of Ca and uptake of Mg and Fe (Christidis, 1998), which

results in the co-existence of both di- and trioctahedral species. As weathering proceeds, the precursor of trioctahedral smectite becomes thermodynamically unstable due to reduced Mg concentrations in the pore fluid and, especially, the more acidic conditions in the middle to upper soil profile (Kittrick, 1973), resulting in alteration of smectite to kaolinite and/or illite. This transformation is often considered to be a solid-state process in which the tetrahedral sheets of smectite are stripped away (Ryan and Huertas, 2009; Hong et al., 2012). Decomposition of the tetrahedral sheets leads to a redistribution of elements marked primarily by the loss of Si and gain of Al. In acidic conditions, Al from interlayer sites will be mobilized, and increasing Al concentrations in the pore fluid will favor the diffusion of Al between external solution and interlayer space of smectite and thus the replacement of octahedral Mg by Al (Mavris et al., 2011; Cheng et al., 2022). In addition, Fe^{2+} in dioctahedral sites of the parent mineral is likely to be oxidized to Fe^{3+} during transformation of smectite to mixed-layer K/S, analogous to the oxidation of Fe^{2+} during transformation of dioctahedral biotite to neoformed clay phases during early-stage weathering (Jeong and Kim, 2003; Cheng et al., 2022).

Given the low K content of the picrite basalt bedrock, the notably higher K concentrations in the Dali soil imply efficient retention by neoformed clay phases of K released from the basalt through weathering. The increase in K content coupled with an increase of illite in the upper soil profile suggests that K is incorporated in the interlayer of illite due to smectite illitization in response to more advanced weathering and pedogenic processes (Table 2). K enrichment of the topsoil has been widely observed in weathering soil profiles developed on basalts elsewhere (e.g., Nesbitt and Wilson, 1992; Sheldon, 2003; He et al., 2008), a phenomenon that has been attributed to targeted uptake of K in the deeper soil by plants (Barré et al., 2007; He et al., 2008; Bakker et al., 2019) or to the addition of K-rich aeolian material (Nesbitt and Wilson, 1992; Sheldon, 2003). In the Dali soil profile, the composition of the clay mineral assemblage (i.e., presence of smectite, K/S, I/S, and I/S/K but absence of a mica-like phase) strongly suggests an autochthonous weathering product. However, K-rich aeolian material from the northern Tibetan Plateau is transported via monsoonal winds only as far southward as the zone along the Yangtze River, far from the Dali area in southern China (Qiao et al., 2011; Cheng et al., 2018). The relative accumulation of K in the topsoil of the Dali profile may be ascribed to fertilizer in human land use of mainly maize cultivation, as indicated by the notably higher TOC value, the distinctly black color, and the sharp
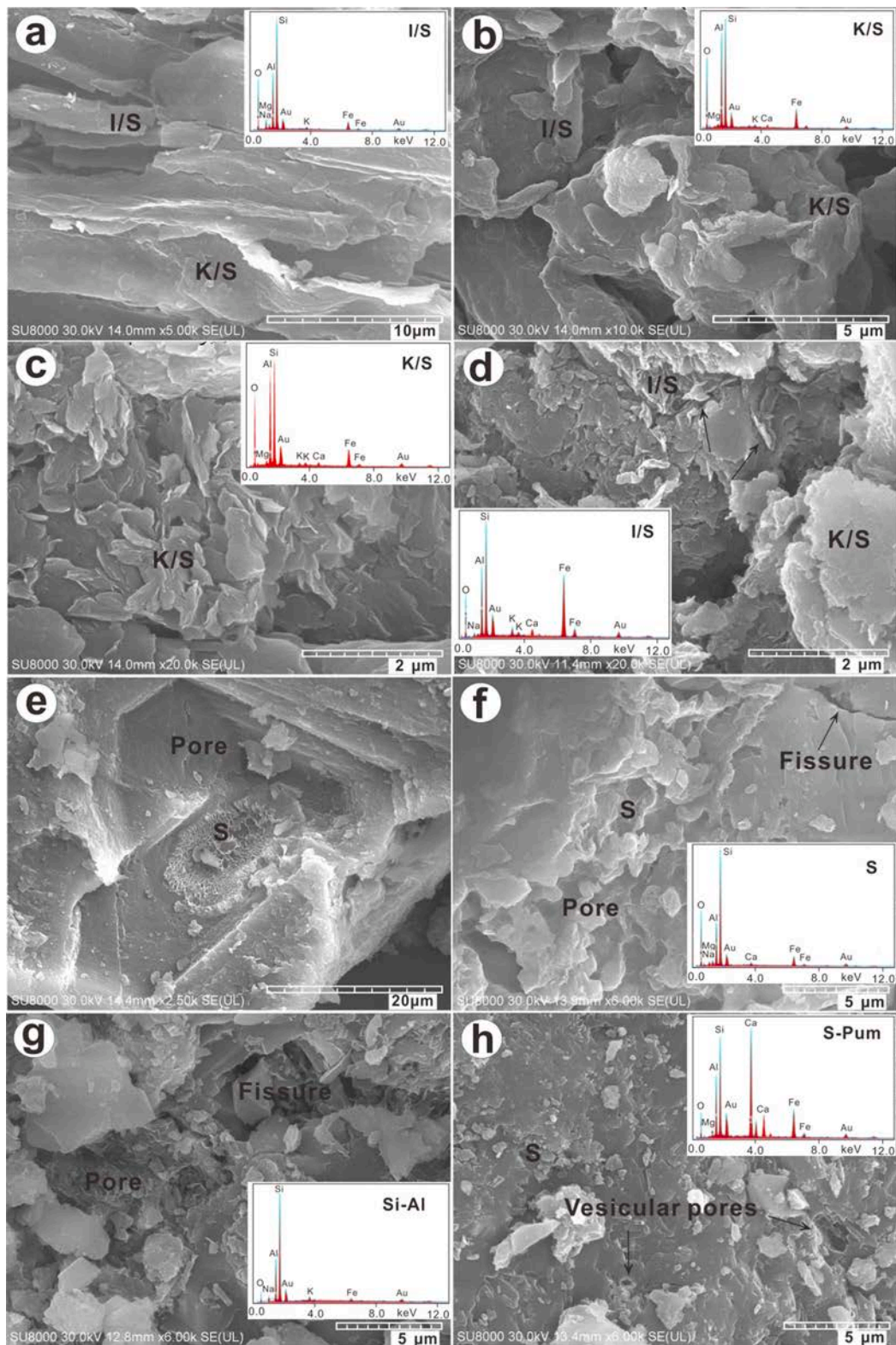
Fig. 7. SEM images of the Dali samples. (a) Poorly-developed pseudo-hexagonal and plate-like grains indicating presence of K/S and I/S (SiO_2/Al_2O_3 value of 1.74) clays in Layer 1 (DYX-01); (b) Relatively well-crystalline K/S (SiO_2/Al_2O_3 value of 1.23) and I/S clay minerals in Layer 2 (DYX-05); (c) K/S clays (SiO_2/Al_2O_3 value of 1.25) with curled edges indicating relatively weak kaolinization in the Layer 3 (DYX-09); (d) K/S and I/S (SiO_2/Al_2O_3 value of 1.65) clays with ragged outlines confined by basalt grains showing replacement by clay minerals, and I/S clays with curled edges in pores indicating clay formation in free spaces in Layer 4 (DYX-16); (e),(f),(g) Typical honeycombed polygonal smectite (SiO_2/Al_2O_3 value of 2.96) in pore space indicating crystallization from porewater solution in Layer 4 (DYX-16), and fissures and pores in the bedrocks and some of them filling with Si-Al aggregates (SiO_2/Al_2O_3 value of 3.12) as reflected by the EDS (DYX-18). (h) Vesicular structure and poorly-developed fine-grained smectite associated pumpellyite showing chemical compositions of mainly Si, Ca, Al, and Fe in the bedrock (DYX-18). (I/S: mixed-layer illite/smectite; K/S: mixed-layer kaolinite/smectite; S: smectite; Pum: pumpellyite).
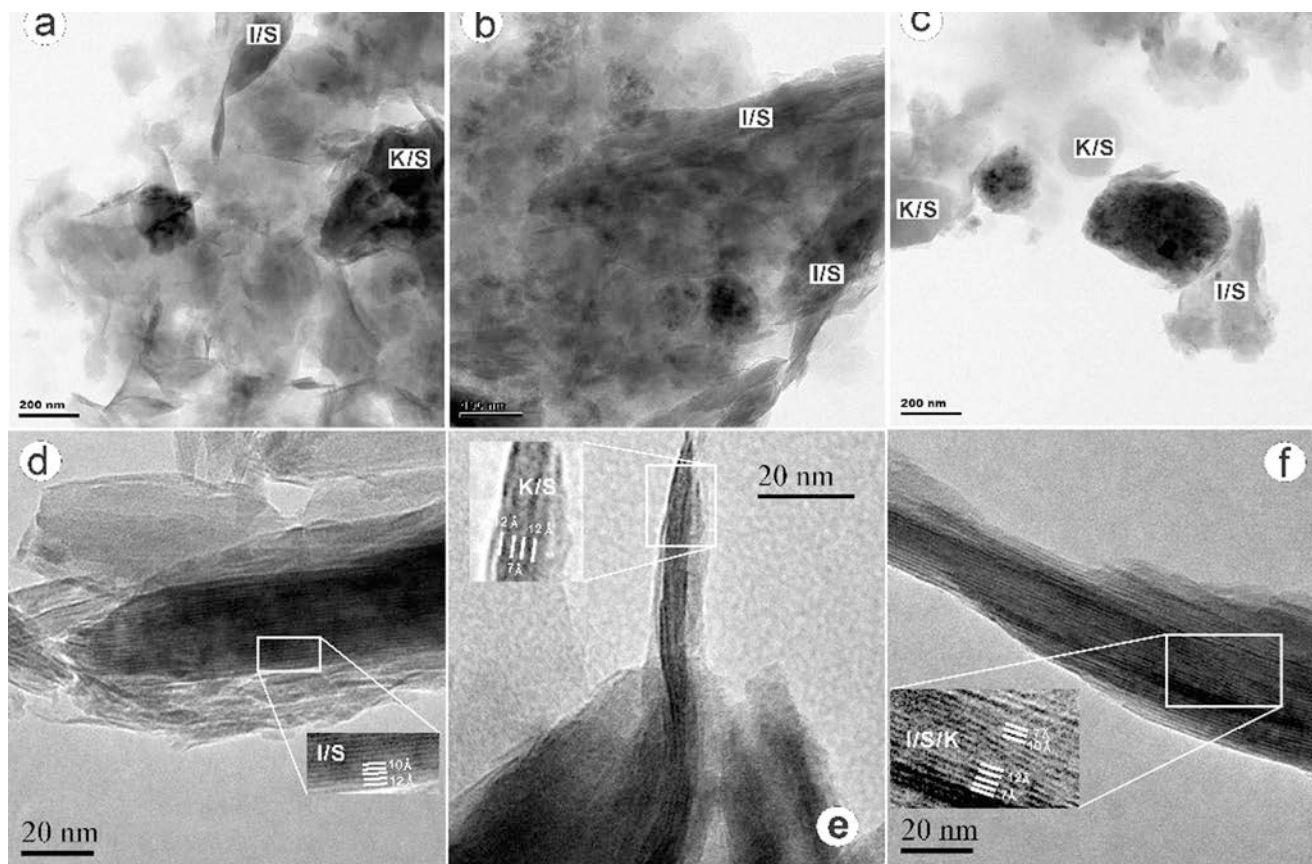
Fig. 8. HRTEM observations showing the morphology and interstratified lattice fringes of clay minerals of the Dali soil. (a) Wave-shaped morphology of K/S and I/S (DYX-13, Layer 4); (b) An elongate and relatively straight morphology indicative of strong illitization of I/S (DYX-13, Layer 4); (c) Euhedral pseudo-hexagonal outlines showing strong kaolinization of K/S (DYX-5, Layer 2); (d) I/S clay with interstratified 12-, 10-, and 7-Å lattice fringes (DYX-5, Layer 2); (e) K/S clay showing interstratification of 12-Å with 7-Å layer (DYX-13, Layer 4); (f) Interstratified 12-, 10-, and 7-Å lattice fringes characteristic of mixed smectite, illite, and kaolinite layers (I/S/K) (DYX-13, Layer 4).

boundary between the underlying soil layer (Table 1; Fig. 2), and also to the recycling uptake of K by plants from deeper soil horizons. These processes result in K-fixing in illitic minerals and facilitate illitization of smectite, consistent with much more illitic clays in the topsoil (He et al., 2008; Bakker et al., 2019).

5.2. Distribution of major elements in the basalt-derived soils

Development of soil during weathering of basalts is generally accompanied by the loss of mobile elements such as Si, Ca, and Mg, and by significant accumulation of immobile elements such as Fe and Al (Chesworth et al., 1981; Eggleton et al., 1987; Markússon and Stefánsson, 2011; Babechuk et al., 2014). Al is regarded as the most immobile element during chemical weathering of volcanic materials (Chesworth et al., 1981; Pokrovsky et al., 2005; Hong et al., 2019).

The major element oxides SiO_2, MgO, and CaO were gained in the Layer 4 and lost from other soil layers at Dali. TiO_2 and TFe_2O_3 were gained throughout the soil profile except for a few samples showing losses in Layers 2 and 3. MnO, Na_2O, and K_2O were mostly gained, whereas P_2O_5 was generally lost during weathering (Fig. 9).

The notable accumulation of SiO_2 in Layer 4 was likely associated with chemical weathering of altered picrite basalt bedrock, since weathering of fresh basalt is generally characterized by dissolution of silicates and glass as well as the formation of a poorly-crystalline Si-Al product (Daux et al., 1994; Dekayir and El-Maataoui, 2001). Kaolinization and illitization of smectite is a desilication process, and the notable decreases in Mg, Ca, and Mn in the upper profile were associated with the transformation of tri- and dioctahedral clay minerals to

dioctahedral clay species. The strong depletions of SiO_2, CaO, and MgO in Layers 1, 2, and 3 at Dali were related to abundant formation of advanced weathering phases, as the previously formed (i.e., early) weathering products transformed over time to thermodynamically more stable phases such as K/S and I/S clays and well-crystalline Fe-oxy-hydroxides (Glasmann and Simonson, 1985; May et al., 1986; Righi et al., 1999; Liivamägi et al., 2018). P_2O_5 displays a general decrease upwards, with depletion in Layers 2 and 3 that were probably due to biogeochemical P cycling and/or leaching in view of the eluvial condition and high TOC content of the soil (Wang et al., 2022).

Al_2O_3, Fe_2O_3, and TiO_2 show gradual increases upward through the Dali weathering profile (Table 3; Figs. 6 and 9). The bedrock has a CIA value of 32, and the soil profile shows a progressive change in CIA from 54 in Layer 4 to 85 in the Layer 2, indicating a general upward increase in weathering intensity. However, the gains or losses of Fe_2O_3, MnO, and TiO_2 relative to Al_2O_3 are inconsistent with these CIA values. Fe_2O_3, MnO, and TiO_2 are markedly enriched in Layer 1 and Layer 4 but relatively depleted in Layers 2 and 3 compared to Al_2O_3. This indicates that, although chemical weathering caused loss of mobile components and gain of immobile components, the fluxes of Fe_2O_3, MnO, and TiO_2 and their sites of concentration or redistribution differed from those of Al_2O_3.

The mineralogical index of alteration (MIA) is used to estimate the transformation ratio of a primary mineral into its equivalent alteration mineral. MIA values of < 20, 20–60, and > 60 reflect incipient, intermediate, and intense to extreme mineralogical transformations, respectively (Voicu et al., 1997). Layer 4 in the lower soil profile has MIA of 8–18, consistent with the absence of K/S clays and the
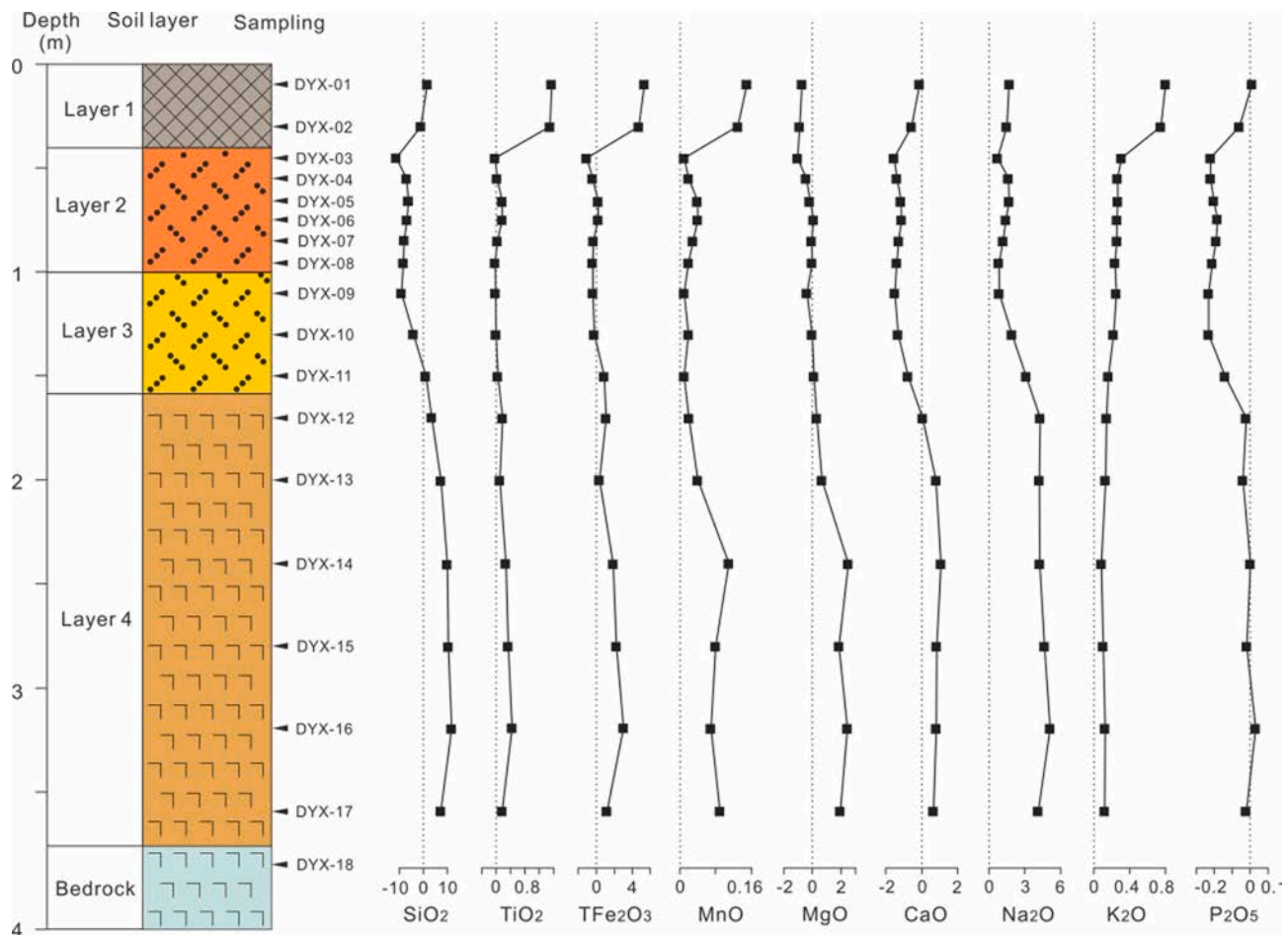
Fig. 9. Gain or loss of major elements through the Dali soil profile.

preservation of a certain amount of pumpellyite (Fig. 3). Layers 1, 2, and 3 have notably higher MIA of 35 to 71, although only a few values are > 60, corresponding to greater amounts of K/S in those samples. This MIA pattern indicates a general upward increase in weathering intensity and an intermediate degree of mineralogical alteration for the Dali soil profile as a whole.

Similarly to the MIA index, the Dali soil profile exhibits dominantly incipient (CIA = 50–60) to intermediate (CIA = 60–80) chemical weathering intensities, with only a few samples in Layers 2 and 3 showing intense weathering (CIA > 80) (Table 3). The moderate weathering intensities indicate that kaolinization did not go to completion, consistent with clay mineral assemblages consisting mainly of K/S, smectite, and minor I/S species (Caner et al., 2014; Van Ranst et al., 2020). The presence of plagioclase also indicates relatively limited chemical weathering (Table 3; Fig. 3), allowing preservation of certain labile elements (e.g., Ca, Mg, Na, and K) (Berry et al., 1983; He et al., 2008). Although Na is largely retained within the soil profile, its lower layers contain notably more Na_2O (3.57–4.84 %) than its upper layers (1.06–2.42 %), indicating a degree of Na loss. Na exhibits a gain-or-loss trend that is markedly similar to that of Ca (Fig. 6), indicating that their weathering behaviour is strongly linked. Covariation of Na and Ca reflects a common provenance in plagioclase, a mineral that is relatively well preserved in the lower soil profile where the bedrock has undergone only incipient weathering. Similar upward decreases in Na and Ca suggest their congruent removal due to chemical weathering of plagioclase in the upper soil profile. In particular, all soil layers exhibit the same clay mineral assemblage consisting of smectite and mixed-layer K/S and I/S clays, with K/S and I/S clays increasing and smectite decreasing toward the top of the profile (Table 2; Fig. 4).

Zr and Ti are also considered to be the least mobile elements during weathering of basalts (Eggleton et al., 1987; Nesbitt and Wilson, 1992; Arslan et al., 2006). At Dali, soil samples from Layer 4 to Layer 1 have nearly uniform Zr/TiO_2 ratios of 0.008–0.011, indistinguishable from that of the basalt bedrock (0.008) (Table 3). This observation suggests that the weathering profile represents mainly or exclusively *in situ* weathering products, with little to no addition of allochthonous Fe- and K-rich aeolian materials. However, the soil profile contains notably more K compared to its bedrock (Fig. 9). The formation of pumpellyite and smectite in the bedrock suggests that this igneous rock has experienced a hydrothermal alteration when buried by the overlying Maokou Formation and the Wujiaping Formation (Mevel, 1981; Inoue and Utada, 1991; Hou et al., 1999; He et al., 2003; Mirabella et al., 2005; De Rosa et al., 2016). The notable more K in the soil profile is probably related to incorporation of K by illite in response to more advanced weathering and pedogenic processes.

The immobile oxides TFe_2O_3 and TiO_2 are markedly enriched in the topsoil at Dali (Fig. 9), consistent with the greater amounts of hematite and anatase in this layer (Fig. 3). The concentration of these immobile components is often attributed to the loss of mobile elements during intense weathering (Brantley et al., 2007; Perez-Fodich and Derry, 2019). However, in iron-rich duricrusts in the tropical regions of Brazil, the concentration of these immobile components may involve the direct role of microorganisms (Levett et al. 2020). Microbial-induced weathering in iron-rich duricrusts promotes the dissolution of iron, aluminum, and titanium oxide minerals, allowing limited migration at a mineral scale before reprecipitation. Soluble ferrous iron readily reprecipitates in the pore spaces in proximity to microorganisms due to changes in oxidation potential of the solution (Levett et al., 2020). Aluminum

migrated as a soluble cation due to changes in solution pH and/or organic chemistry, resulting in the observed depletion of aluminum and the relative concentrations of titanium and iron in the topsoil (Ramanaidou, 2009). The Dali topsoil has notably higher TiO_2/Al_2O_3 (0.195–0.198) compared to Layers 2, 3, and 4 (0.103–0.132) (Table 3), suggesting that depletion of aluminum may have occurred during the weathering process.

6. Conclusions

The distribution of authigenic minerals in the Dali basalt-derived soil is largely defined by soil layers related to pedogenesis. Smectite decreases upward from 39 to 64 % in Layer 4 to 12 % in the topsoil, whereas I/S and K/S increase upward from 0 to 2 % to 24 % and from 36 to 59 % to 64 %, respectively. Clay phases from the saprolite have a mixture of di- and trioctahedral species, whereas those from the middle to upper soil profile have a uniformly dioctahedral structure. I/S clays are characterized by interstratification of 12-Å smectite with 10-Å illite layers, whereas K/S clays exhibit intercalation of 12-Å smectite and 7-Å kaolinite layers. The intercalation of 12-, 10-, and 7-Å clay layers represents mixed-layer I/S/K clays. The significantly greater abundance of K/S clay relative to I/S clay in the saprolite implies that kaolinization of smectite took place at an early stage after smectite formation, whereas illitization of smectite occurred during a later stage characterized by increased leaching. However, the processes of kaolinization and illitization of smectite overlapped during the developmental history of the soil.

Desilication and K-fixation of smectite occurred with advanced weathering, but the absence of discrete kaolinite and illite and the lack of detectable gibbsite in the soils indicate that the Dali soils formed in a weathering environment of only moderate intensity. Both the immobile oxides (TFe_2O_3 and TiO_2) and a mobile component (K_2O) are markedly concentrated in the topsoil. The concentration of K in the weathering profile was potentially related to incorporation of K in the interlayer of illite due to smectite illitization in response to more advanced weathering and pedogenic processes, and the relative accumulation of K in the topsoil probably results from fertilizer in land use and recycling of K by plants.

Declaration of Competing Interest

The authors declare that they have no known competing financial interests or personal relationships that could have appeared to influence the work reported in this paper.

Data availability

Data will be made available on request.

Acknowledgments

References

Alexander, G.C., Heal, H.G., 1974. Ion-exchange properties and possible applications of weathered Antrim basalts. J. Chem. Technol. Biotechnol. 24, 387–400.

Arslan, M., Kadir, S., Abdioğlu, E., Kolaylı, H., 2006. Origin and formation of kaolin minerals in saprolite of Tertiary alkaline volcanic rocks, Eastern Pontides, NE Turkey. Clay Miner. 41, 597–617.

Babechuk, M.G., Widdowson, M., Kamber, B.S., 2014. Quantifying chemical weathering intensity and trace element release from two contrasting basalt profiles, Deccan Traps, India. Chem. Geol. 363, 56–75.

Bain, D.C., Ritchie, P.F.S., Clark, D.R., Duthie, D.M.L., 1980. Geochemistry and mineralogy of weathered basalt from Morvern, Scotland. Mineral. Mag. 43, 865–872.

Bakker, E., Lanson, B., Findling, N., Wander, M.M., Hubert, F., 2019. Mineralogical differences in a temperate cultivated soil arising from different agronomic processes and plant K-uptake. Geoderma 347, 210–219.

Bakker, L., Lowe, D.J., Jongmans, A.G., 1996. A micromorphological study of pedogenic processes in an evolutionary soil sequence formed on Late Quaternary rhyolitic tephra deposits, North Island, New Zealand. Quat. Int. 34–36, 249–261.

Barbera, V., Raimondi, S., Egli, M., Plotze, M., 2008. The influence of weathering processes Mediterranean on labile and stable organic matter in volcanic soils. Geoderma 143, 191–205.

Barré, P., Velde, B., Abbadie, L., 2007. Dynamic role of "illite-like'' clay minerals in temperate soils: facts and hypotheses. Biogeochemistry 82, 77–88.

Berry, L.G., Mason, B., Dietrich, R.V., 1983. Mineralogy-Concepts, Descriptions. Determinations. W. H, Freeman and Company, San Francisco, p. 561.

Brantley, S.L., Goldhaber, M., Ragnarsdottir, K.V., 2007. Crossing disciplines and scales to understand the critical zone. Elements 3, 307–314.

Campodonico, V.A., Pasquini, A.I., Lecomte, K.L., García, M.G., Depetris, P.J., 2019. Chemical weathering in subtropical basalt-derived laterites: a mass balance interpretation (Misiones, NE Argentina). Catena 173, 352–366.

Caner, L., Radtke, L.M., Vignol-Lelarge, M.L., Inda, A.V., Bortoluzzi, E.C., Mexias, A.S., 2014. Basalt and rhyo-dacite weathering and soil clay formation under subtropical climate in southern Brazil. Geoderma 235–236, 100–112.

Chen, J.M., Gong, G., Zhao, L.Q., Sun, X.C., 2000. Determination of cation exchange capacity of expansive soils. Rock Miner. Anal. 19 (2), 152–154 in Chinese with English abstract.

Cheng, F., Hong, H.L., Bae, C.J., Li, Z., Algeo, T.J., Huang, S.M., Cheng, L.L., Fang, Q., 2018. Geochemical and detrital zircon U-Pb geochronological constraints on provenance of the Xiaomei red earth sediments (Bose Basin, Guangxi Province, southern China). Palaeogeogr. Palaeoclimatol. Palaeoecol. 2018 (510), 49–62.

Cheng, S., Hong, H.L., Ji, K.P., Li, F., Wang, X.H., 2022. New insight into biotite weathering in the subtropic Tongcheng granite regolith, Hubei Province, South China. Appl. Clay Sci. 224, 106518.

Chesworth, W., 1973. The parent rock effect in the genesis of soil. Geoderma 10, 215–225.

Chesworth, W., Duou, J., Larroque, P., 1981. The weathering of basalt and relative mobilities of the major elements at Belbex, France. Geochim. Cosmochim. Acta 45, 1235–1243.

Christidis, G.E., 1998. Comparative study of the mobility of major and trace elements during alteration of an andesite and a rhyolite to bentonite, in the islands of Milos and Kimolos, Aegean, Greece. Clays Clay Miner. 46, 379–399.

Courtillot, V., Jaupart, C., Manighetti, I., Tapponnier, P., Besse, J., 1999. On causal links between flood basalts and continental breakup. Earth Planet. Sci. Lett. 166, 177–195.

Curi, N., Franzmeier, D.P., 1987. Effect of parent rocks on chemical and mineralogical properties of some Oxisols in Brazil. Soil Sci. Soc. Am. J. 51, 153–158.

Curtin, D., Smillie, G.W., 1981. Composition and origin of smectite in soils derived from basalt in Northern Ireland. Clays Clay Miner. 29, 277–284.

Daux, V., Crovisier, J.L., Hemond, C., Petit, J.C., 1994. Geochemical evolution of basaltic rocks subjected to weathering: fate of the major elements, rare earth elements, and thorium. Geochim. Cosmochim. Acta 58, 4941–4954.

De Rosa, R., Donato, P., Scarciglia, F., 2016. On the origin and post-depositional history of widespread massive ash deposits: The case of Intermediate Brown Tuffs (IBT) of Lipari (Aeolian Islands, Italy). J. Volcanol. Geoth. Res. 327, 135–151.

Deepthy, R., Balakrishnan, S., 2005. Climatic control on clay mineral formation: evidence from weathering profiles developed on either side of the Western Gnats. J. Earth Syst. Sci. 114, 545–556.

Dekayir, A., El-Maataoui, M., 2001. Mineralogy and geochemistry of supergene alteration of an alkali basalt from the Middle Atlas, Morocco. J. Afr. Earth Sc. 32, 619–633.

Eggleton, R.A., Foudoulis, C., Varkevisser, D., 1987. Weathering of basalt: changes in rock chemistry and mineralogy. Clays Clay Miner. 35, 161–169.

Glassmann, J.R., Simonson, G.M., 1985. Alteration of basalt in soils of Western Oregon. Soil Sci. Soc. Am. J. 49, 262–273.

He, Y., Li, D.C., Velde, B., Yang, Y.F., Huang, C.M., Gong, Z.T., Zhang, G.L., 2008. Clay minerals in a soil chronosequence derived from basalt on Hainan Island, China and its implication for pedogenesis. Geoderma 148, 206–212.

He, B., Xu, Y.G., Xiao, L., Wang, K.M., Sha, S.L., 2003. Generation and spatial distribution of the Emeishan Large Igneous Province: New evidence from stratigraphic records. Acta Geol. Sin. 77, 194–201 in Chinese with English abstract.

Hillier, S., 2000. Accurate quantitative analysis of clay and other minerals in sandstones by XRD: comparison of a Rietveld and a reference intensity ratio (RIR) method and the importance of sample preparation. Clay Miner. 35, 291–302.

Hong, H.L., Zhang, N., Li, Z., Xue, H.J., Xia, W.C., Yu, N., 2008. Clay mineralogy across the P/T boundary of the Xiakou section, China: evidence of clay provenance and environment. Clays Clay Miner. 56, 131–143.

Hong, H.L., Churchman, G.J., Gu, Y.S., Yin, K., Wang, C.W., 2012. Kaolinite–smectite mixed-layer clays in the Jiujiang red soils and their climate significance. Geoderma 173–174, 75–83.

Hong, H.L., Fang, Q., Wang, C.W., Churchman, G.J., Zhao, L.L., Gong, N.N., Yin, K., 2017. Clay mineralogy of altered tephra beds and facies correlation between the Permian-Triassic boundary stratigraphic sets, Guizhou, South China. Appl. Clay Sci. 143, 10–21.

Hong, H.L., Algeo, T.J., Fang, Q., Zhao, L.L., Ji, K.P., Yin, K., Wang, C.W., Cheng, S.L., 2019. Facies dependence of the mineralogy and geochemistry of altered volcanic ash beds: An example from Permian-Triassic transition strata in southwestern China. Earth Sci. Rev. 190, 58–88.

Hou, Z.Q., Lu, J.R., Wang, Y.L., Xia, L.Q., Li, H.Y., Guo, L.J., 1999. Emei large igneous province: characteristics and origin. Geol. Rev. 45 (Supp.), 885–891 in Chinese with English abstract.

Inoue, A., Utada, M., 1991. Pumpellyite and related minerals from hydrothermally altered rocks at the Kalmikta area, northern Honshu, Japan. Canadian Mineral. 29, 255–270.

Jackson, M.L., 1978. Soil Chemical Analysis. Self-Published, University of Wisconsin, Madison, U.S.A.

Jeong, G.Y., Kim, H.B., 2003. Mineralogy, chemistry, and formation of oxidized biotite in the weathering profile of granitic rocks. Am. Mineral. 88, 352–364.

Jiang, K., Qi, H.W., Hu, R.Z., 2018. Element mobilization and redistribution under extreme tropical weathering of basalts from the Hainan Island, South China. J. Asian Earth Sci. 158, 80–102.

Kantor, W., Schwertmann, U., 1974. Mineralogy and genesis of clays in red-black toposequences in Kenya. J. Soil Sci. 25, 67–78.

Kittrick, J.A., 1973. Mica-derived vermiculites as unstable intermediates. Clays Clay Miner. 21, 479–488.

Lessovaia, S.N., Plötze, M., Inozemzev, S., Goryachkin, S., 2016. Traprock transformation into clayey materials in soil environments of the Central Siberian Plateau, Russia. Clays Clay Miner. 64, 668–676.

Levett, A., Vasconcelos, P.M., Gagen, E.J., Rintoul, L., Spier, C., Guagliardo, P., Southam, G., 2020. Microbial weathering signatures in lateritic ferruginous duricrusts. Earth Planet. Sci. Lett. 538, 116209.

Li, G.J., Hartmann, J., Derry, L.A., West, A.J., You, C.F., Long, X.Y., Zhan, T., Li, L.F., Li, G., Qiu, W.H., Li, T., Liu, L.W., Chen, Y., Ji, J.F., Zhao, L., Chen, J., 2016. Temperature dependence of basalt weathering. Earth and Planetary Science Letters 443, 59–69.

Liivamägi, S., Środoń, J., Bojanowski, M.J., Gerdes, A., Stanek, J.J., Williams, L., Szczerba, M., 2018. Paleosols on the Ediacaran basalts of the East European Craton: a unique record of paleoweathering with minimum diagenetic overprint. Precambr. Res. 316, 66–82.

Ma, Y.J., Luo, J.X, Jiang, M.Y., Yang, D.Y., 1999. The weathering and evolution of soil ferralite minerals in the South China. Acta Sedimentologica Sinica, 17 (Supp.), 681-686 (in Chinese text with English abstract).

Markússon, S.H., Stefánsson, A., 2011. Geothermal surface alteration of basalts, Krýsuvík Iceland—Alteration mineralogy, water chemistry and the effects of acid supply on the alteration process. J. Volcanol. Geoth. Res. 206, 46–59.

Mavris, C., Ploetze, M., Mirabella, A., Giaccai, D., Valboa, G., Egli, M., 2011. Clay mineral evolution along a soil chronosequence in an Alpine proglacial area. Geoderma 165, 106–117.

Mevel, C., 1981. Occurrence of pumpellyite in hydrothermally altered basalts from the Vema fracture zone (mid-Atlantic ridge). Contrib. Miner. Petrol. 76, 386–393.

Mirabellal, A., Egli, M., Raimondi, S., Giaccai, D., 2005. Origin of clay minerals in soils on pyroclastic deposits in the island of Lipari (Italy). Clays Clay Miner. 53, 409–421.

Nesbitt, H.W., Wilson, R.E., 1992. Recent chemical weathering of basalts. Am. J. Sci. 292, 740–777.

Orhan, D., Hüseyin, S., 2018. Effect of toposequences on geochemical mass balance and clay mineral formation in soils developed on basalt parent material under subhumid climate condition. Indian J. Geo-Marine Sci. 47, 1809–1820.

Perez-Fodich, A., Derry, L.A., 2019. Organic acids and high soil CO_2 drive intense chemical weathering of Hawaiian basalts: insights from reactive transport models. Geochim. Cosmochim. Acta 249, 173–198.

Pokrovsky, O.S., Schott, J., Kudryavtzev, D.I., Dupre, B., 2005. Basalt weathering in Central Siberia under permafrost conditions. Geochim. Cosmochim. Acta 69, 5659–5680.

Prudèncio, M.I., Sequeira Braga, M.A., Paquet, H., Waerenborgh, J.C., Pereira, L.C.J., Gouveia, M.A., 2002. Clay mineral assemblages in weathered basalt profiles from central and southern Portugal: climatic significance. Catena 49, 77–89.

Qiao, Y., Hao, Q., Peng, S., Wang, Y., Li, J., Liu, Z., 2011. Geochemical characteristics of the eolian deposits in southern China, and their implications for provenance and weathering intensity. Palaeogeogr. Palaeoclimatol. Palaeoecol. 308, 513–523.

Ramanaidou, E.R., 2009. Genesis of lateritic iron ore from banded iron-formation in the Capanema mine (Minas Gerais, Brazil). Aust. J. Earth Sci. 56, 605–620.

Rasmussen, C., Dahlgren, R.A., Southard, R.J., 2010. Basalt weathering and pedogenesis across an environmental gradient in the southern Cascade Range, California, USA. Geoderma 154, 473–485.

Reynolds Jr., R.C., Reynolds III, R.C., 1996. NEWMOD-for-Windows. The Calculation of One-dimensional X-ray Diffraction Patterns of Mixed-layered Clay Minerals, Hanover, New Hampshire.

Righi, D., Terribile, F., Petit, S., 1999. Pedogenic formation of kaolinite-smectite mixed layers in a soil toposequence developed from basaltic parent material in Sardinia (Italy). Clays Clay Miner. 47, 505–514.

Ryan, P.C., Huertas, F.J., 2009. The temporal evolution of pedogenic Fe–smectite to Fe–kaolin via interstratified kaolin–smectite in a moist tropical soil chronosequence. Geoderma 151, 1–15.

Sheldon, N.D., 2003. Pedogenesis and geochemical alteration of the Picture Gorge subgroup, Columbia River basalt, Oregon. Geol. Soc. Am. Bull. 115, 1377–1387.

Singer, A., Ármannsson, H., 1999. Weathering of basic magmatic rocks under Mediterranean conditions. Geochemistry of the Earth's Surface International Symposium, 1999.

Sulieman, M.M., Sh Sallam, A., Brevik, E.C., Al-farraj, A.S., 2020. Investigation of the clay minerals composition of soils derived from basalt parent materials in the Early Miocene to Early Pleistocene on the Arabian Shield using multiple techniques: implications for paleoclimatic conditions. Environ. Earth Sci. 79, 297.

Van Der Gaast, S.J., Mizota, C., Jansen, J.H.F., 1986. Curved smectite in soils from volcanic ash in Kenya and Tanzania: a low-angle X-ray powder diffraction study. Clays Clay Miner. 34, 665–671.

Van Ranst, V., Kips, P., Mbogoni, J., Mees, F., Dumon, M., Delvaux, B., 2020. Halloysite-smectite mixed-layered clay in fluvio-volcanic soils at the southern foot of Mount Kilimanjaro. Tanzania. Geoderma 375, 114527.

Vingiani, S., Righi, D., Petit, S., Terribile, F., 2004. Mixed-layer kaolinite-smectite minerals in a red-black soil sequence from basalt in Sardinia (Italy). Clays Clay Miner. 52, 473–483.

Voicu, G., Bardoux, M., Voicu, D., 1997. Mineralogical norm calculations applied to tropical weathering profiles. Mineral. Mag. 61, 185–196.

Wang, R.Z., Yang, J.J., Liu, H.Y., Sardans, J., Zhang, Y.H., Wang, X.B., Wei, C.Z., Lu, X.T., Dijkstra, F.A., Jiang, Y., Han, X.G., Penuelas, J., 2022. Nitrogen enrichment buffers phosphorus limitation by mobilizing mineral-bound soil phosphorus in grasslands. Ecology 103, e3616.

Wilson, S.G., Lambert, J.J., Nanzyo, M., Dahlgren, R.A., 2017. Soil genesis and mineralogy across a volcanic lithosequence. Geoderma 285, 301–312.

Ziegler, K., Hsieh, J.C.C., Chadwick, O.A., Kelly, E.F., Hendricks, D.M., Savin, S.M., 2003. Halloysite as a kinetically controlled end product of arid-zone basalt weathering. Chem. Geol. 202, 461–478.